RESEARCH ARTICLE | NOVEMBER 16 2022

A characterization of plasma properties of a heterogeneous magnetized low pressure discharge column

Hossein Mehrpour Bernety ; Luc S. Houriez ; Jesse A. Rodríguez ; Benjamin Wang ; Mark A. Cappelli

AIP Advances 12, 115220 (2022)
https://doi.org/10.1063/5.0124845

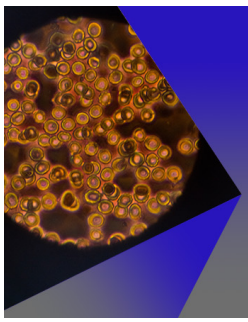

A characterization of plasma properties of a heterogeneous magnetized low pressure discharge column

Cite as: AIP Advances 12, 115220 (2022); doi: 10.1063/5.0124845
Submitted: 8 September 2022 • Accepted: 31 October 2022 •
Published Online: 16 November 2022

Hossein Mehrpour Bernety,[a] Luc S. Houriez, Jesse A. Rodríguez, Benjamin Wang, and Mark A. Cappelli

AFFILIATIONS

Department of Mechanical Engineering, Stanford University, Stanford, California 94305, USA

[a]Author to whom correspondence should be addressed: bernety@stanford.edu

ABSTRACT

An approach is presented for characterizing heterogeneous magnetized plasma discharge tubes through the scattering of electromagnetic plane waves. Here, we formulate the analytical problem of electromagnetic scattering from a gyrotropic plasma column. The scattering accounts for the heterogeneous composition of the cylindrical discharge plasma and facilitates determining its propensity for gyrotropic scattering, particularly when electron collisional damping may be prevalent. The analytical results are validated using computational simulations. Scattered fields from the magnetized plasma are measured experimentally, and, by comparing the analytical and experimental results, the unknown parameters of the discharge, i.e., characteristic plasma and electron collisional damping frequencies, are determined. The technique is relatively straight-forward to use and removes the need for commercial computational electromagnetic simulations when experimental data on scattering characteristics of such cylindrical discharge plasmas are available.

I. INTRODUCTION

The problem of electromagnetic scattering by canonical objects is essential to designing miscellaneous devices in various frequency regimes.[1] The geometry and material properties of a given object affect the resulting scattered fields, which can be used directly for design purposes or to elicit information in inverse scattering problems. As a result, understanding electromagnetic scattering from objects enables us to find ways for re-routing waves and controlling them in the desired fashion.

In recent years, there has been much interest in canceling the scattered fields from a given object in order for realizing practical invisibility cloaks.[2–5] In addition, one can leverage the scattering from small inclusions to make metamaterials and achieve various properties not found in nature by arranging them in periodic arrays,[6] such as negative refraction[7–11] and near-zero permittivity.[12–16] If the periodicity of such arrays is comparable to the wavelength at the operation frequency, one can construct photonic crystals.[17–20] In some cases, topological properties[21–24] may arise from such photonic crystals.

The metamaterial and photonic crystals described in the literature are most often assembled out of metallic and dielectric structures. Graphene has been of interest to researchers for designing tunable devices in the low terahertz (THz) range of frequencies.[25] Here, we focus on another class of materials, gaseous plasmas, as potential structural elements that have novel scattering properties, particularly when magnetized. Such gaseous plasmas can have relatively low electron collisional scattering rates and their properties, i.e., plasma frequency can be tuned by varying the plasma density. Such a tunable material can be of interest in the development of various microwave devices. When biased with a constant magnetic field, a plasma's permittivity, or dielectric constant, has an anisotropic tensor form and, as a result, presents a gyrotropic response to an incident electromagnetic wave.[26–28] Electromagnetic dispersion bands of a bulk magnetized plasma can be topologically non-trivial (TNT).[24] By juxtaposing such a TNT material with an isotropic material, one can achieve exotic properties like unidirectional interfacial waves that are highly confined to the boundary and immune to back-scattering, not normally seen at the boundary between two topologically trivial materials. This unidirectional feature leads

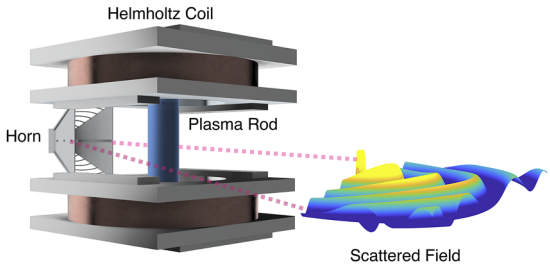

FIG. 1. Configuration for examining the scattering from a magnetized plasma rod.

to non-reciprocity and enables the design of reconfigurable and tunable one-way waveguides.

To facilitate the design and analysis of such unique structures made of gyrotropic, gaseous plasma discharge tubes, one requires an estimation of their plasma and electron collisional damping frequencies. Although various approximate techniques exist, such as the measurements of the detuning of microwave cavity modes,[29] which have been used for non-magnetized cases or indirectly from the measurements of discharge voltage and current,[30] these methods are not appropriate when the discharge is magnetized. In addition, in our very recently published paper,[31] we have confirmed the gyrotropic behavior of a magnetized discharge tube. There, using another indirect technique, the unknown parameters have been initially estimated from discharge operating conditions via BOLSIG+,[32,33] and then, we performed many computational simulations back and forth to improve our estimation. As a result, a more direct and appropriate characterization technique for magnetized plasma tubes is needed.

The problem addressed by this paper is to resolve the issue of characterizing a large class of plasma discharge tubes for the purpose of determining their largely unknown parameters, i.e., plasma frequency (electron density) and electron collisional scattering frequency, particularly when these discharges are strongly magnetized. We leverage the analytical solution of electromagnetic scattering from a heterogeneous discharge tube to characterize these heterogeneous discharges and to determine their unknown, scattering-relevant parameters for the purpose of using them as an element in the construction of other complex structures. An experimental configuration that we compare the model and simulations to is depicted in Fig. 1. The plasma rod is considered to be oriented along the axis of an externally applied magnetic bias generated by Helmholtz coils. A horn antenna is used for launching the incident fields with a propagation vector largely perpendicular to the bias axis. We compare scattered fields to those measured in the plane passing through the center of the rod. The magnetized rod is modeled as a three-layer heterogeneous medium, accounting for the quartz envelope and low-density region in the envelope's vicinity.

II. ELECTROMAGNETIC SCATTERING FROM A HETEROGENEOUS MAGNETIZED PLASMA ROD

Our analytical analysis addresses the electromagnetic scattering from the heterogeneous magnetized plasma column shown in Fig. 2. The rod is represented as a three-layer structure consisting of

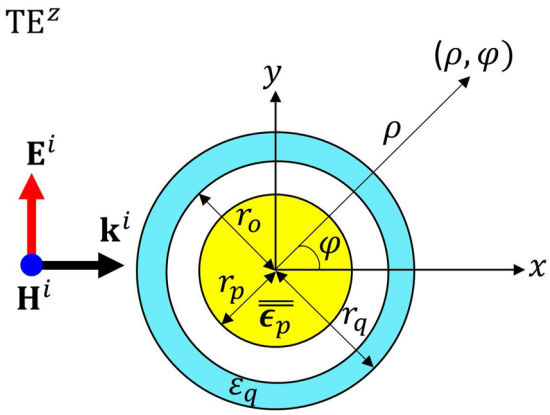

FIG. 2. Schematic of the three-layer cylindrical model of a plasma rod under a normal TE plane wave incidence.

a uniform magnetized plasma core (the yellow region in the figure), surrounded by a thin non-ionized layer (white), and an outer quartz envelope (blue). This representation of the plasma is only approximate because, in reality, there is a smooth transition in plasma density from the core to the very low levels near the quartz wall. It, nevertheless, is a starting point for a comprehensive analytical model that can be expanded to more layers if necessary to account for a gradual decrease in plasma density.

We consider a uniform transverse electric (TE) plane wave traveling along the x-axis normally incident upon the rod in a plane perpendicular to the rod axis, as shown in the figure. The incident magnetic field, $\mathbf{H}^i$, can be expressed as an infinite sum of cylindrical wave functions:[34]

$$\mathbf{H}^i = \hat{\mathbf{z}}\, H_z^i = \hat{\mathbf{z}}\, e^{-jk_0 x} = \hat{\mathbf{z}}\, e^{-jk_0\rho\,\cos\varphi} = \hat{\mathbf{z}} \sum_{n=-\infty}^{\infty} j^{-n} J_n(k_0\rho)\, e^{jn\varphi}, \tag{1}$$

with k_0 representing the free space wave number, φ is the scattering angle measured from the axis of the plasma rod, ρ is the distance from the axis, and J_n is the Bessel function of the first kind. The incident electric field, $\mathbf{E}^i$, can then be written as

$$\mathbf{E}^i = \frac{1}{j\omega\varepsilon_0} \nabla \times \mathbf{H}^i = E_\rho^i \hat{\boldsymbol{\rho}} + E_\varphi^i \hat{\boldsymbol{\varphi}}, \tag{2a}$$

with ε_0 representing the permittivity of vacuum and

$$E_\rho^i = \frac{1}{j\omega\varepsilon_0\rho} \sum_{n=-\infty}^{\infty} n j^{-n+1} J_n(k_0\rho)\, e^{jn\varphi}, \tag{2b}$$

$$E_\varphi^i = \frac{-1}{j\omega\varepsilon_0} \sum_{n=-\infty}^{\infty} j^{-n} J_n'(k_0\rho)\, e^{jn\varphi}, \tag{2c}$$

and

$$J_n'(k_0\rho) = \frac{\partial J_n(k_0\rho)}{\partial\rho}; k_0 = 2\pi f\sqrt{\varepsilon_0\mu_0}, \tag{2d}$$

which can be evaluated using the relation

$$J_n'(\alpha x) = \frac{\partial J_n(\alpha x)}{\partial x} = \alpha J_{n-1}(\alpha x) - \frac{n}{x} J_n(\alpha x). \tag{2e}$$

We can express the scattered magnetic and electric fields, $\mathbf{H}^s$ and $\mathbf{E}^s$, in terms of the Hankel functions of the second kind, $H_n^{(2)}$, i.e.,

$$\mathbf{H}^s = \hat{\mathbf{z}} H_z^s = \hat{\mathbf{z}} \sum_{n=-\infty}^{\infty} a_n H_n^{(2)}(k_0\rho)\ e^{jn\varphi}, \tag{3}$$

$$\mathbf{E}^s = \frac{1}{j\omega\varepsilon_0} \nabla \times \mathbf{H}^s = E_\rho^s \hat{\boldsymbol{\rho}} + E_\varphi^s \hat{\boldsymbol{\varphi}}, \tag{4a}$$

with a_n being coefficients of the expansion to be determined, and

$$E_\rho^s = \frac{1}{j\omega\varepsilon_0\rho} \sum_{n=-\infty}^{\infty} jn a_n H_n^{(2)}(k_0\rho)\ e^{jn\varphi}, \tag{4b}$$

$$E_\varphi^s = \frac{-1}{j\omega\varepsilon_0} \sum_{n=-\infty}^{\infty} a_n H_n^{(2)'}(k_0\rho)\ e^{jn\varphi}, \tag{4c}$$

and

$$H_n^{(2)'}(k_0\rho) = \frac{\partial H_n^{(2)}(k_0\rho)}{\partial \rho}. \tag{4d}$$

Here, we use the relation

$$H_n^{(2)'}(\alpha x) = \frac{\partial H_n^{(2)}(\alpha x)}{\partial x} = \alpha H_{n-1}^{(2)}(\alpha x) - \frac{n}{x} H_n^{(2)}(\alpha x). \tag{4e}$$

The fields inside the quartz tube ($\mathbf{E}^q$ and $\mathbf{H}^q$), with relative permittivity of ε_q, are expressed as

$$\mathbf{H}^q = \hat{\mathbf{z}} \sum_{n=-\infty}^{\infty} [b_n J_n(k_q\rho) + c_n Y_n(k_q\rho)] e^{jn\varphi}, \tag{5}$$

$$\mathbf{E}^q = \frac{1}{j\omega\varepsilon_0\varepsilon_q} \nabla \times \mathbf{H}^q = E_\rho^q \hat{\boldsymbol{\rho}} + E_\varphi^q \hat{\boldsymbol{\varphi}}, \tag{6a}$$

where $k_q = k_0\sqrt{\varepsilon_q}$, Y_n is the Bessel function of the second kind, and

$$E_\rho^q = \frac{1}{j\omega\varepsilon_0\varepsilon_q\rho} \sum_{n=-\infty}^{\infty} jn[b_n J_n(k_q\rho) + c_n Y_n(k_q\rho)] e^{jn\varphi}, \tag{6b}$$

$$E_\varphi^q = \frac{-1}{j\omega\varepsilon_0\varepsilon_q} \sum_{n=-\infty}^{\infty} \left[b_n J_n'(k_q\rho) + c_n Y_n'(k_q\rho)\right] e^{jn\varphi}. \tag{6c}$$

Here, b_n and c_n are the coefficients of this expansion and are also to be determined. The fields inside the non-ionized layer ($\mathbf{E}^o$ and $\mathbf{H}^o$) are represented as

$$\mathbf{H}^o = \hat{\mathbf{z}} \sum_{n=-\infty}^{\infty} [B_n J_n(k_0\rho) + C_n Y_n(k_0\rho)] e^{jn\varphi}, \tag{7}$$

$$\mathbf{E}^o = \frac{1}{j\omega\varepsilon_0} \nabla \times \mathbf{H}^o = E_\rho^o \hat{\boldsymbol{\rho}} + E_\varphi^o \hat{\boldsymbol{\varphi}}. \tag{8a}$$

Here, B_n and C_n are unknown coefficients, and

$$E_\rho^o = \frac{1}{j\omega\varepsilon_0\rho} \sum_{n=-\infty}^{\infty} jn[B_n J_n(k_0\rho) + C_n Y_n(k_0\rho)] e^{jn\varphi}, \tag{8b}$$

$$E_\varphi^o = \frac{-1}{j\omega\varepsilon_0} \sum_{n=-\infty}^{\infty} \left[B_n J_n'(k_0\rho) + C_n Y_n'(k_0\rho)\right] e^{jn\varphi}. \tag{8c}$$

Finally, the fields inside the magnetized plasma ($\mathbf{E}^p$ and $\mathbf{H}^p$) with a tensor relative permittivity, $\bar{\bar{\varepsilon}}_p$, given by[35]

$$\bar{\bar{\varepsilon}}_p = \begin{bmatrix} \varepsilon_t & j\varepsilon_g & 0 \\ -j\varepsilon_g & \varepsilon_t & 0 \\ 0 & 0 & \varepsilon_z \end{bmatrix}, \tag{9}$$

can be expressed as

$$\mathbf{H}^p = \hat{\mathbf{z}} H_z^p = \hat{\mathbf{z}} \sum_{n=-\infty}^{\infty} d_n J_n(k_p\rho)\ e^{jn\varphi}, \tag{10}$$

$$\mathbf{E}^p = \frac{1}{j\omega\varepsilon_0} \bar{\bar{\varepsilon}}_p^{-1} \cdot \left(\nabla \times \mathbf{H}^p\right) = E_\rho^p \hat{\boldsymbol{\rho}} + E_\varphi^p \hat{\boldsymbol{\varphi}}, \tag{11a}$$

where d_n is an unknown coefficient of expansion, and

$$E_\rho^p = \frac{1}{j\omega\varepsilon_0\rho} \frac{1}{\varepsilon_p} \left[\sum_{n=-\infty}^{\infty} jn d_n J_n(k_p\rho)\ e^{jn\varphi}\right] + \frac{1}{j\omega\varepsilon_0} \frac{j}{\varepsilon_p'} \times \left[\sum_{n=-\infty}^{\infty} d_n J_n'(k_p\rho)\ e^{jn\varphi}\right], \tag{11b}$$

$$E_\varphi^p = \frac{1}{j\omega\varepsilon_0\rho} \frac{j}{\varepsilon_p'} \left[\sum_{n=-\infty}^{\infty} jn d_n J_n(k_p\rho)\ e^{jn\varphi}\right] - \frac{1}{j\omega\varepsilon_0} \frac{1}{\varepsilon_p} \times \left[\sum_{n=-\infty}^{\infty} d_n J_n'(k_p\rho)\ e^{jn\varphi}\right]. \tag{11c}$$

The elements of $\bar{\bar{\varepsilon}}_p$ are

$$\varepsilon_t = 1 - \frac{\omega_p^2(\omega - j\nu_c)}{\omega[(\omega - j\nu_c)^2 - \omega_{ce}^2]}, \tag{12a}$$

$$\varepsilon_g = -\frac{\omega_p^2\omega_{ce}}{\omega[(\omega - j\nu_c)^2 - \omega_{ce}^2]}, \tag{12b}$$

and

$$\varepsilon_z = 1 - \frac{\omega_p^2}{\omega(\omega - j\nu_c)}. \tag{12c}$$

Here, ω_p, ω_{ce}, and ω are the plasma, electron cyclotron, and field frequencies, respectively, and the wave damping rate is attributed to electron scattering with the background gas at a rate ν_c. The inverse of the relative permittivity tensor can be expressed as

$$\bar{\bar{\varepsilon}}_p^{-1} = \begin{bmatrix} \frac{\varepsilon_t}{\varepsilon_t^2 - \varepsilon_g^2} & \frac{-j\varepsilon_g}{\varepsilon_t^2 - \varepsilon_g^2} & 0 \\ \frac{j\varepsilon_g}{\varepsilon_t^2 - \varepsilon_g^2} & \frac{\varepsilon_t}{\varepsilon_t^2 - \varepsilon_g^2} & 0 \\ 0 & 0 & \frac{1}{\varepsilon_z} \end{bmatrix} = \begin{bmatrix} \frac{1}{\varepsilon_p} & \frac{-j}{\varepsilon_p'} & 0 \\ \frac{j}{\varepsilon_p'} & \frac{1}{\varepsilon_p} & 0 \\ 0 & 0 & \frac{1}{\varepsilon_z} \end{bmatrix}. \tag{13}$$

To solve for all unknown coefficients a_n, b_n, c_n, B_n, C_n, and d_n, one applies the corresponding boundary conditions that enforce the continuity of the tangential electric and magnetic fields at $\rho = r_p$, $\rho = r_o$, and $\rho = r_q$. The details are given in the Appendix. Once the coefficient a_n is determined, the scattered fields are computed using (3) and (4a).

III. COMPUTATIONAL SIMULATIONS AND COMPARISONS TO ANALYTICAL RESULTS

Computational simulations are carried out for comparison to the analytical results using the full-wave electromagnetic simulator, CST Microwave Studio (CST MWS).[36] While one can use both time-domain (TD) and frequency-domain (FD) solvers in CST MWS for the simulation of structures that include non-magnetized plasmas, only the FD solver is configurable for the case of magnetized, gyrotropic plasma. Considering the coordinates defined in Fig. 2, the Open (Add Space) boundary conditions are used in the x- and y-directions. The plasma rod is taken to have a finite length, L, along the z-direction. The boundary conditions at the minimum and maximum z-values are set to be periodic to mimic the scattering from an infinitely long rod. The structure is then excited with a plane wave, as shown in Fig. 3.

For a 3D object, the radar cross section (RCS or σ_{3D}) is defined as[1,34]

$$\sigma_{3D}(\theta,\varphi) = \lim_{r\to\infty} 4\pi r^2 \frac{\|\mathbf{H}^s\|^2}{\|\mathbf{H}^i\|^2}, \tag{14}$$

where (r,θ,φ) are the spherical coordinates, and $\|\mathbf{H}^i\|$ and $\|\mathbf{H}^s\|$ are the magnitudes of the incident and scattered vector magnetic fields, respectively. For a given 2D object under normal incidence, the scattering width (σ_{2D}) can be defined as[1,34]

$$\sigma_{2D}(\varphi) = \lim_{\rho\to\infty} 2\pi\rho \frac{\|\mathbf{H}^s\|^2}{\|\mathbf{H}^i\|^2}, \tag{15}$$

where ρ is the radial parameter in cylindrical coordinates shown in Fig. 2.

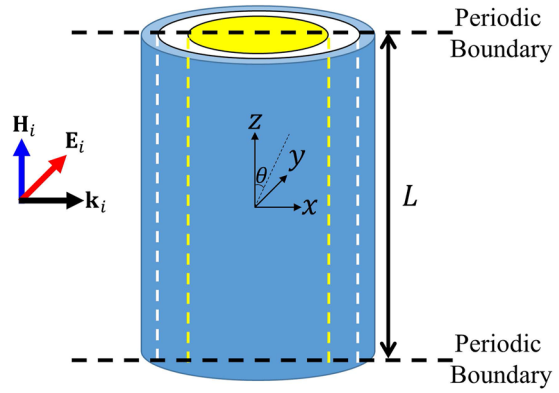

FIG. 3. Parameters and orientation for simulations of a heterogeneous plasma rod under normal TE plane wave incidence.

If a finite cylinder of length L is exposed to an oblique plane wave with the angle of incidence, θ_i, one can relate σ_{3D} and σ_{2D} through[37]

$$\sigma_{3D}(\theta,\varphi) = \sigma_{2D}(\varphi)\cdot\frac{2L^2}{\lambda}\cdot\left(\frac{\sin X}{X}\right)^2, \tag{16a}$$

where

$$X = \frac{k_0 L}{2}(\cos\theta_i + \cos\theta), \tag{16b}$$

and $\lambda = 2\pi/k_0$ is the wavelength at the desired incident field frequency. As a result, for the case of normal incidence, i.e., $\theta_i = 90^\circ$, the observation angle will also be $\theta = 90^\circ$, and we have

$$\sigma_{3D}(\theta = 90^\circ,\varphi) = \sigma_{2D}(\varphi)\cdot\frac{2L^2}{\lambda}. \tag{17}$$

The CST simulation is performed for a rod with a finite length, L, allowing the determination of σ_{3D}^{sim}. Then, the scattering width normalized to the wavelength can be found from

$$\frac{\sigma_{2D}(\varphi)}{\lambda} = \frac{\sigma_{3D}(\theta = 90^\circ,\varphi)}{2L^2}. \tag{18}$$

We compare these computational simulations to the scattering predicted by the analytical results (Sec. II) using (15).

With the analytical and computational analyses of the electromagnetic scattering from a magnetized plasma rod established, we can then utilize these tools to analyze the scattering properties of a discharge tube for both non-magnetized and magnetized plasma cases. The considered plasma rod is a custom-fabricated fluorescent ultraviolet (UV) discharge source with $r_p = 4.6$ mm, $r_o = 6.5$ mm, and $r_q = 7.5$ mm. The relative permittivity of the quartz layer is $\varepsilon_q = 3.75$.

A. Non-magnetized plasma with symmetry

The non-magnetized plasma rod is simply a special case of the magnetized one with $\omega_{ce} = 0$. Accordingly, one can use the aforementioned three-layer model, but the relative permittivity of the plasma column changes to the scalar (isotropic) relative permittivity, i.e.,

$$\varepsilon_t = \varepsilon_z = 1 - \frac{\omega_p^2}{\omega(\omega - j\nu_c)}, \tag{19a}$$

$$\varepsilon_g = 0. \tag{19b}$$

We consider the case of a plasma frequency $f_p = \omega_p/2\pi = 6.35$ GHz, and a field frequency $f = \omega/2\pi = 0.6 f_p = 3.81$ GHz. The analytical and computational simulation results of the bistatic scattering width, normalized to the wavelength, are shown in Fig. 4 for different values of the collision frequency, ν_c. These plots show that the analytical model is in good agreement with computational simulations and that by increasing the collision frequency (damping of the wave by losses within the plasma rod), the bistatic width is reduced. This is also seen by examining the effect of loss on the magnitude of the scattering coefficients, a_n. As shown in Fig. 5, the scattering coefficients diminish in magnitude as the collisional loss

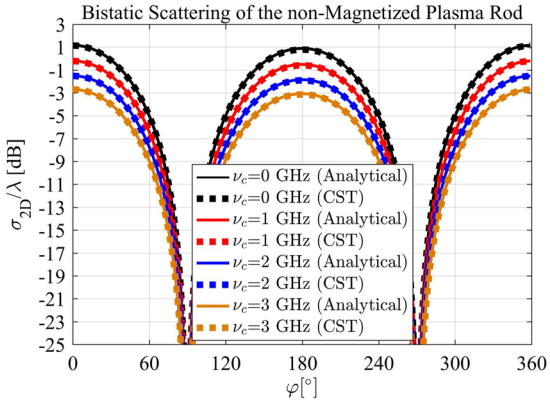

FIG. 4. Comparison of an analytical model to computational simulations for the scattering of a non-magnetized ($\omega_{ce} = 0$) rod under normal TE plane wave incidence.

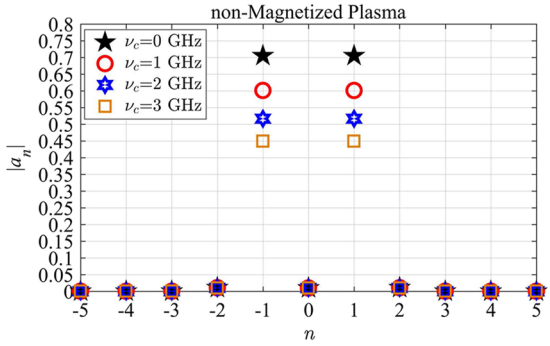

FIG. 5. Magnitude of the scattering coefficients, a_n, for the non-magnetized ($\omega_{ce} = 0$) plasma discharge tube with a sub-wavelength radius.

increases. It is noteworthy that because the radius of the plasma rod is small compared to the wavelength, a_{-1} and a_1 will be the only dominant scattering coefficients.

As expected, in the absence of a magnetic field, the scattering pattern shown in Fig. 4 will be symmetric with respect to the plane of incidence, due to the fact that the scattering coefficients are symmetric in magnitude, as illustrated in Fig. 5. Note that if n is even, we have $a_n = a_{-n}$, and if n is odd, we have $a_n = -a_{-n}$.

B. Magnetized plasma with broken symmetry

Here, we consider the electromagnetic scattering from a magnetized plasma discharge tube of the same properties considered above, but with an electron cyclotron frequency, $f_{ce} = \omega_{ce}/2\pi = 1.27$ GHz. The analytical model for the bistatic scattering width, normalized to the wavelength, is compared to computational simulations in Fig. 6 for different values of the electron collision frequency, ν_c. We see that similar to the case of the non-magnetized rod, increasing the collisional-induced loss leads to a reduction in the bistatic scattering width of the rod. We also see, as expected, that the magnetic field breaks the symmetry of the scattering pattern. Unlike the non-magnetized case, where the maximum scattering is

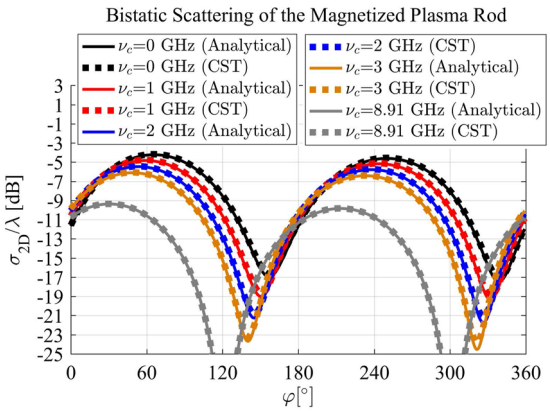

FIG. 6. Comparison of the analytical model to computational simulations for a magnetized rod ($f_{ce} = \omega_{ce}/2\pi = 1.27$ GHz) under a normal TE plane wave incidence.

found to be at $\varphi = 0°$ and $\varphi = 180°$, here, we see the maximum in the peaks at $\varphi = 66°$ and $\varphi = 250°$ for the idealized case with $\nu_c = 0$ GHz. In examining the scattering coefficients, a_n, in Fig. 7, we see that for the dominant, odd coefficients $|a_{-1}| \neq |a_1|$.

Electron collisional damping plays a significant role in the modeled asymmetric scattering. We can see that if the electron collision frequency is increased to a value of $\nu_c = 8.91$ GHz, we have $|a_{-1}| = |a_1|$, as is the case of the non-magnetized rod. However, as apparent in Fig. 6, the scattering pattern has maxima at $\varphi = 30°$ and $\varphi = 213°$ and not at the angles seen for the non-magnetized case. This is because although the magnitudes of the coefficients are the same, they differ in their real and imaginary contributions. For this high collisional-induced damping case, the dominant coefficients are $a_{-1} = 0.153 - j0.139$ and $a_1 = 0.058 + j0.199$. We emphasize that to recover symmetry, the condition that $|a_{-n}| = |a_n|$ is a necessary but not sufficient condition. We find that the collisional damping must be about an order of magnitude larger than the electron cyclotron frequency for the scattering pattern to approach that of the non-magnetized case, but then there is a substantial (20 dB) reduction in the scattering intensity, as seen from the trend in the figure. In practice, such high damping is generated when the gas pressure is

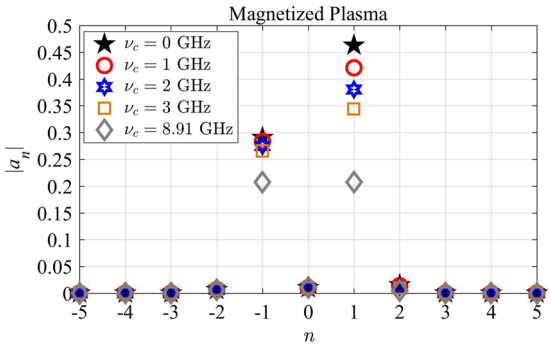

FIG. 7. Magnitude of the scattering coefficients, a_n, for the magnetized ($f_{ce} = \omega_{ce}/2\pi = 1.27$ GHz) plasma discharge tube with a sub-wavelength radius.

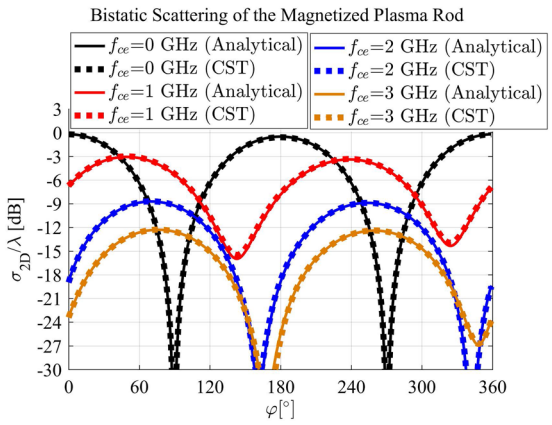

FIG. 8. Comparison of the analytical model to computational simulations for a magnetized rod under a normal TE plane wave incidence. Here, ν_c = 1 GHz.

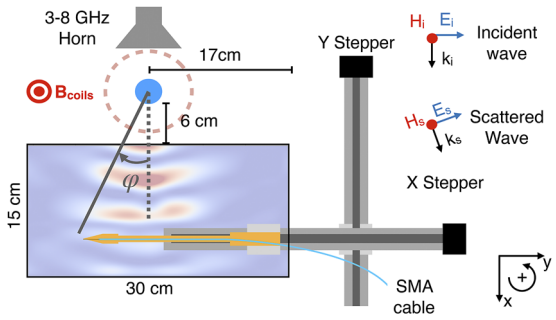

FIG. 9. Top view schematic of the experimental setup, reproduced from Houriez *et al.*, "Experimental study of electromagnetic wave scattering from a gyrotropic gaseous plasma column," Appl. Phys. Lett. **120**, 223101 (2022),[31] with the permission of AIP Publishing. The field map shown is actual data recorded at 4.42 GHz for a non-magnetized plasma discharge tube.

higher or when the electron gyroradius is comparable to the inner diameter of the discharge.

In Fig. 8, we examine how the applied magnetic bias alters the bistatic scattering, by comparing the results of the analytical model for various values of $\omega_{ce} = 2\pi f_{ce} = eB_o/m_e$, which is linearly dependent on the magnetic field, B_0. Here, m_e and e are the electron mass and charge, respectively. In the figure, the applied magnetic field is varied from B_0 = 0 mT to B_0 = 107.2 mT. Within this range, it is seen that by increasing the field, the angles of maximum scattering increase from $\varphi = 0^\circ$ and $\varphi = 180^\circ$ to $\varphi = 76^\circ$ and $\varphi = 259^\circ$, respectively. However, such broken symmetry results in an almost 12 dB reduction of the maximum bistatic width for a constant collision frequency of ν_c = 1 GHz.

IV. COMPARISON TO EXPERIMENTS

Experimental results of the scattered fields from a magnetized plasma rod were presented in a recent paper[31] and are only briefly reviewed here. The experimental set-up is illustrated schematically in Fig. 9. A broadband horn launches an incident electromagnetic wave in the 3–8 GHz frequency range onto a gaseous plasma rod positioned within Helmholtz coils with the rod axis aligned with the magnetic field, which has a value of 47 mT. The wave scattered from the rod is detected by a robot field mapper[38] equipped with a receiver antenna.

The plasma rod consists of a quartz tube with an inner and outer diameter of 13 and 15 mm, respectively, a length of 290 mm, and is filled with ~250 Pa of argon and a small amount of mercury. The discharge is driven at 33 kHz (AC) and with 144 V peak to peak voltage. The root-mean-square discharge current is 298 mA. The plasma density can be tuned[39] by varying the discharge voltage, but here, we compare the analytical model to scattering data collected only for the above conditions.

The field robot maps a 15 × 30 cm^2 area with a 0.75 cm step size, and probe signals are processed for amplitude and phase using an HP 8722D Vector Network Analyzer, allowing reconstruction of the scattered wavefronts. The field inset shown in Fig. 9 is the actual recorded scattered data in the absence of a magnetic bias for a frequency of 4.42 GHz.

As described in our previous study,[31] we first recorded the scattering from a non-magnetized plasma, which confirmed symmetry when the magnets are off. In computing the scattered fields, probe data are recorded with and without the plasma activated and subtracted to isolate the scattered contributions. The Poynting vector of the scattered field is computed at each position over the scanned domain. The scattered field is then mapped for an upward oriented magnetic field (B+) and a downward oriented magnetic field (B-) to confirm a gyrotropic scattering response. Figure 10(a) shows the corresponding wave fronts measured for a frequency of 4.42 GHz, mapped over the same spatial region depicted in the inset to Fig. 9. We see that there is a clear asymmetry in the scattering induced by the magnetized plasma, a confirmation of the active gyrotropic response. For an upward oriented (B+) field, the scattered field is steered toward the left, and for a downward oriented (B−) field, a right-directed steering is observed, breaking the symmetry seen when the magnetic field is turned off.

We now examine the three layer analytical model's capacity to reproduce experimental scattering and assess the agreement to experiments when plasma properties are varied within a range expected based on past studies. An optimization algorithm systematically varies ω_p and ν_c until the model predictions for the scattered fields and corresponding angle-dependent power is in agreement with the measurements. For our discharge and B-field conditions, this optimization generates a plasma frequency, $\omega_p = 5.28 \times 10^{10}$ rad/s, and an electron collisional damping rate of ν_c = 1.34 GHz that best reproduces the experimental result. The analytical scattered field maps for 4.42 GHz field frequency are shown in Fig. 10(b) and are in good qualitative agreement with the experimental maps shown in Fig. 10(a) when using these optimal plasma parameters. The scattered power is computed at every angle φ of the experimental wavefronts by integrating the Poynting vector along a given φ. Figure 10(c) presents the corresponding scattered power in the (B−) and the (B+) configurations from both the experimental and analytical data shown in Figs. 10(a) and 10(b), respectively. The scattered power peaks at angles of approximately ±20. Quantitative agreement

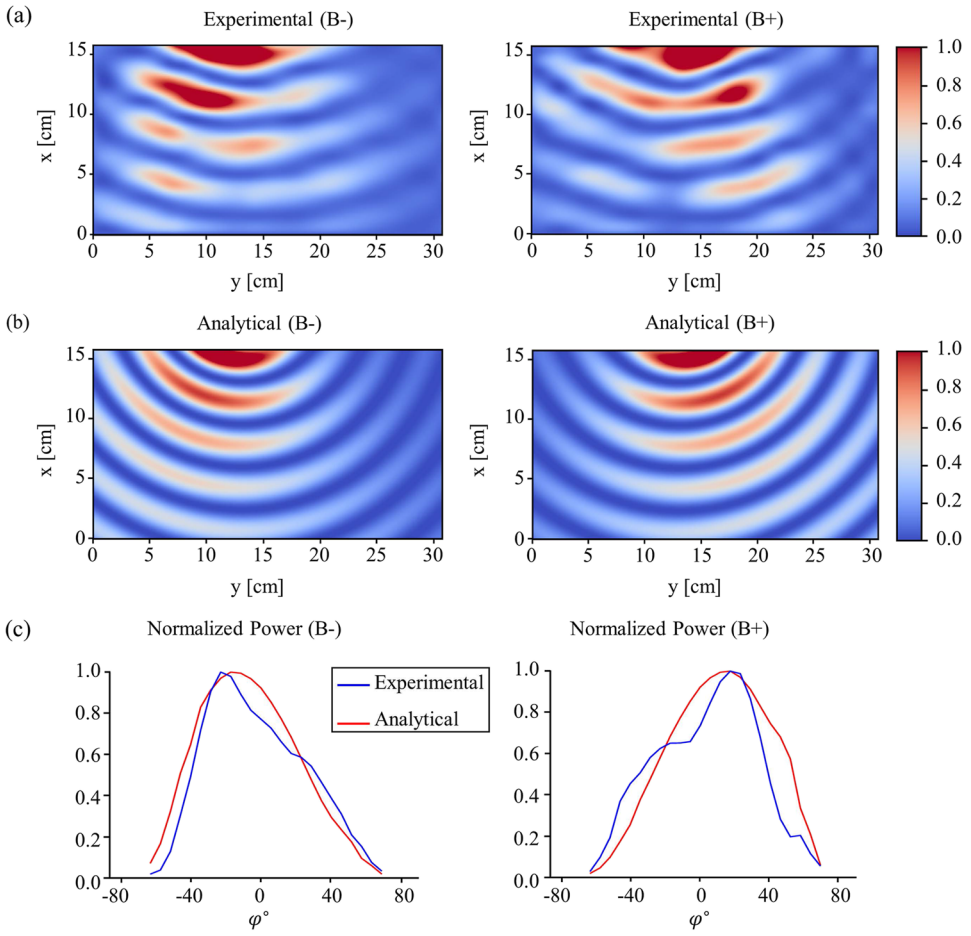

FIG. 10. (a) Experimental scattering measurements for the magnetized plasma rod with the two magnetic field directions, B− (left) and B+ (right). (b) Predicted scattering using the analytical model with $\omega = 2.78 \times 10^{10}$ rad/s, $\omega_{ce} = 8.4 \times 10^{9}$ rad/s, $\omega_p = 5.28 \times 10^{10}$ rad/s, and $\nu_c = 1.34$ GHz. (c) Normalized scattered power derived from experiments (blue curves) and the analytical model (red curves) as a function of angle, φ, in degrees. The experimental results are reproduced from Houriez *et al.*, "Experimental study of electromagnetic wave scattering from a gyrotropic gaseous plasma column," Appl. Phys. Lett. **120**, 223101 (2022),[31] with the permission of AIP Publishing.

is seen in the angular dependence of scattered power, as illustrated in Fig. 10(c), for the estimated plasma parameters.

V. SUMMARY

This paper introduces a straightforward method for characterizing a large class of plasma discharge tubes for the purpose of determining their largely unknown parameters, i.e., plasma frequency (electron density) and electron collisional scattering frequency, particularly when these discharges are strongly magnetized. The proposed method leverages the problem of electromagnetic scattering from magnetized discharge tubes and enables us to estimate their unknown parameters by comparing them with the experimental results of the scattered fields. The technique precludes the need for computational electromagnetic resources for determining scattering parameters for this configuration and can be applied to discharge tubes of varying diameters or sizes. This exercise provides a basis for evaluating such discharge tubes in the construction of novel gyrotropic plasma metamaterials and topologically non-trivial magnetized plasma structures.

ACKNOWLEDGMENTS

This research is partially supported by the Air Force Office of Scientific Research through a Multi-University Research Initiative (MURI) under Grant No. FA9550-21-1-0244, with Dr. Mitat Birkan as the Program Manager. J.A.R. acknowledges support by the U.S. Department of Energy, Office of Science, Office of Advanced Scientific Computing Research, Department of Energy Computational Science Graduate Fellowship under Award No. DE-SC0019323. L.S.H. acknowledges the support of the Stanford France Center for Interdisciplinary Studies.

AUTHOR DECLARATIONS

Conflict of Interest

The authors have no conflicts to disclose.

Author Contributions

Hossein Mehrpour Bernety: Conceptualization (equal); Data curation (equal); Formal analysis (equal); Investigation (equal); Methodology (equal); Software (equal); Supervision (equal); Validation

(equal); Visualization (equal); Writing – original draft (equal); Writing – review & editing (equal). **Luc S. Houriez**: Conceptualization (equal); Data curation (equal); Formal analysis (equal); Investigation (equal); Methodology (equal); Supervision (equal); Validation (equal); Visualization (equal); Writing – original draft (equal); Writing – review & editing (equal). **Jesse A. Rodríguez**: Conceptualization (supporting); Data curation (supporting); Formal analysis (supporting); Investigation (supporting); Methodology (supporting); Supervision (supporting); Validation (supporting); Visualization (supporting); Writing – original draft (supporting); Writing – review & editing (supporting). **Benjamin Wang**: Conceptualization (supporting); Data curation (supporting); Formal analysis (supporting); Investigation (supporting); Methodology (supporting); Supervision (supporting); Validation (supporting); Visualization (supporting); Writing – original draft (supporting); Writing – review & editing (supporting). **Mark A. Cappelli**: Conceptualization (equal); Formal analysis (equal); Funding acquisition (equal); Investigation (equal); Methodology (equal); Project administration (equal); Resources (equal); Supervision (equal); Writing – original draft (equal); Writing – review & editing (equal).

DATA AVAILABILITY

The data that support the findings of this study are available from the corresponding author upon reasonable request.

APPENDIX: MATHEMATICAL FORMULATION

Here, we present the mathematical formulation to determine the unknown coefficients of the electromagnetic scattering problem, i.e., a_n, b_n, c_n, B_n, C_n, and d_n. In doing so, we apply the six boundary conditions as follows:

$$H_z^p\big|_{\rho=r_p} = H_z^o\big|_{\rho=r_p}, \tag{A1}$$

$$E_\varphi^p\big|_{\rho=r_p} = E_\varphi^o\big|_{\rho=r_p}, \tag{A2}$$

$$H_z^o\big|_{\rho=r_o} = H_z^q\big|_{\rho=r_o}, \tag{A3}$$

$$E_\varphi^o\big|_{\rho=r_o} = E_\varphi^q\big|_{\rho=r_o}, \tag{A4}$$

$$H_z^q\big|_{\rho=r_q} = \left[H_z^i + H_z^s\right]\big|_{\rho=r_q}, \tag{A5}$$

$$E_\varphi^q\big|_{\rho=r_q} = \left[E_\varphi^i + E_\varphi^s\right]\big|_{\rho=r_q}. \tag{A6}$$

For each order, n, there exists a matrix equation as

$$\begin{bmatrix} 0 & 0 & 0 & A_{14} & A_{15} & A_{16} \\ 0 & 0 & 0 & A_{24} & A_{25} & A_{26} \\ 0 & A_{32} & A_{33} & A_{34} & A_{35} & 0 \\ 0 & A_{42} & A_{43} & A_{44} & A_{45} & 0 \\ A_{51} & A_{52} & A_{53} & 0 & 0 & 0 \\ A_{61} & A_{62} & A_{63} & 0 & 0 & 0 \end{bmatrix} \cdot \begin{bmatrix} a_n \\ b_n \\ c_n \\ B_n \\ C_n \\ d_n \end{bmatrix} = \begin{bmatrix} 0 \\ 0 \\ 0 \\ 0 \\ j^{-n}J_n(k_0 r_q) \\ j^{-n}J_n'(k_0 r_q) \end{bmatrix}, \tag{A7}$$

where

$$A_{14} = J_n(k_0 r_p), \tag{A8.1}$$

$$A_{15} = Y_n(k_0 r_p), \tag{A8.2}$$

$$A_{16} = -J_n(k_p r_p), \tag{A8.3}$$

$$A_{24} = J_n'(k_0 r_p), \tag{A8.4}$$

$$A_{25} = Y_n'(k_0 r_p), \tag{A8.5}$$

$$A_{26} = -\frac{n}{r_p \varepsilon_p'} J_n(k_p r_p) - \frac{1}{\varepsilon_p} J_n'(k_p r_p), \tag{A8.6}$$

$$A_{32} = J_n(k_q r_o), \tag{A8.7}$$

$$A_{33} = Y_n(k_q r_o), \tag{A8.8}$$

$$A_{34} = -J_n(k_0 r_o), \tag{A8.9}$$

$$A_{35} = -Y_n(k_0 r_o), \tag{A8.10}$$

$$A_{42} = \frac{J_n'(k_q r_o)}{\varepsilon_q}, \tag{A8.11}$$

$$A_{43} = \frac{Y_n'(k_q r_o)}{\varepsilon_q}, \tag{A8.12}$$

$$A_{44} = -J_n'(k_0 r_o), \tag{A8.13}$$

$$A_{45} = -Y_n'(k_0 r_o), \tag{A8.14}$$

$$A_{51} = -H_n^{(2)}(k_0 r_q), \tag{A8.15}$$

$$A_{52} = J_n(k_q r_q), \tag{A8.16}$$

$$A_{53} = Y_n(k_q r_q), \tag{A8.17}$$

$$A_{61} = -H_n^{(2)'}(k_0 r_q), \tag{A8.18}$$

$$A_{62} = \frac{J_n'(k_q r_q)}{\varepsilon_q}, \tag{A8.19}$$

$$A_{63} = \frac{Y_n'(k_q r_q)}{\varepsilon_q}. \tag{A8.20}$$

Here, we introduce the permittivity seen by the penetrated fields for the gyrotropic cylinder,

$$\varepsilon_p = \frac{\varepsilon_t^2 - \varepsilon_g^2}{\varepsilon_t} \rightarrow k_p = k_0\sqrt{\varepsilon_p}. \tag{A9}$$

We also define

$$\varepsilon_p' = \frac{\varepsilon_t^2 - \varepsilon_g^2}{\varepsilon_g}. \tag{A10}$$

REFERENCES

[1] A. V. Osipov and S. A. Tretyakov, *Modern Electromagnetic Scattering Theory with Applications* (John Wiley & Sons, 2017).
[2] J. B. Pendry, D. Schurig, and D. R. Smith, "Controlling electromagnetic fields," Science **312**, 1780–1782 (2006).
[3] A. Alù and N. Engheta, "Achieving transparency with plasmonic and metamaterial coatings," Phys. Rev. E **72**, 016623 (2005).
[4] G. W. Milton and N.-A. P. Nicorovici, "On the cloaking effects associated with anomalous localized resonance," Proc. R. Soc. A **462**, 3027–3059 (2006).
[5] D. Schurig, J. J. Mock, B. J. Justice, S. A. Cummer, J. B. Pendry, A. F. Starr, and D. R. Smith, "Metamaterial electromagnetic cloak at microwave frequencies," Science **314**, 977–980 (2006).
[6] Y. Zhao and A. Alù, "Manipulating light polarization with ultrathin plasmonic metasurfaces," Phys. Rev. B **84**, 205428 (2011).
[7] J. B. Pendry, "Negative refraction makes a perfect lens," Phys. Rev. Lett. **85**, 3966 (2000).
[8] J. B. Pendry and D. R. Smith, "Reversing light with negative refraction," Phys. Today **57**, 37–43 (2004).
[9] J. Yao, Z. Liu, Y. Liu, Y. Wang, C. Sun, G. Bartal, A. M. Stacy, and X. Zhang, "Optical negative refraction in bulk metamaterials of nanowires," Science **321**, 930 (2008).
[10] E. Cubukcu, K. Aydin, E. Ozbay, S. Foteinopoulou, and C. M. Soukoulis, "Negative refraction by photonic crystals," Nature **423**, 604–605 (2003).
[11] H. J. Lezec, J. A. Dionne, and H. A. Atwater, "Negative refraction at visible frequencies," Science **316**, 430–432 (2007).
[12] B. Edwards, A. Alù, M. E. Young, M. Silveirinha, and N. Engheta, "Experimental verification of epsilon-near-zero metamaterial coupling and energy squeezing using a microwave waveguide," Phys. Rev. Lett. **100**, 033903 (2008).
[13] I. Liberal, A. M. Mahmoud, Y. Li, B. Edwards, and N. Engheta, "Photonic doping of epsilon-near-zero media," Science **355**, 1058–1062 (2017).
[14] I. Liberal and N. Engheta, "Near-zero refractive index photonics," Nat. Photonics **11**, 149–158 (2017).
[15] N. Engheta, "Pursuing near-zero response," Science **340**, 286–287 (2013).
[16] N. Kinsey, C. DeVault, A. Boltasseva, and V. M. Shalaev, "Near-zero-index materials for photonics," Nat. Rev. Mater. **4**, 742–760 (2019).
[17] E. Yablonovitch, "Photonic crystals," J. Mod. Opt. **41**, 173–194 (1994).
[18] J. D. Joannopoulos, P. R. Villeneuve, and S. Fan, "Photonic crystals: Putting a new twist on light," Nature **386**, 143–149 (1997).
[19] T. Baba, "Slow light in photonic crystals," Nat. Photonics **2**, 465–473 (2008).
[20] P. P. Sun, R. Zhang, W. Chen, P. V. Braun, and J. G. Eden, "Dynamic plasma/metal/dielectric photonic crystals in the mm-wave region: Electromagnetically-active artificial material for wireless communications and sensors," Appl. Phys. Rev. **6**, 041406 (2019).
[21] Z. Wang, Y. Chong, J. D. Joannopoulos, and M. Soljačić, "Observation of unidirectional backscattering-immune topological electromagnetic states," Nature **461**, 772–775 (2009).
[22] L. Lu, J. D. Joannopoulos, and M. Soljačić, "Topological photonics," Nat. Photonics **8**, 821–829 (2014).
[23] S. Pakniyat, A. M. Holmes, G. W. Hanson, S. A. H. Gangaraj, M. Antezza, M. G. Silveirinha, S. Jam, and F. Monticone, "Non-reciprocal, robust surface plasmon polaritons on gyrotropic interfaces," IEEE Trans. Antennas Propag. **68**, 3718–3729 (2020).
[24] C. Valagiannopoulos, S. A. H. Gangaraj, and F. Monticone, "Zeeman gyrotropic scatterers: Resonance splitting, anomalous scattering, and embedded eigenstates," Nanomater. Nanotechnol. **8**, 1847980418808087 (2018).
[25] P.-Y. Chen, J. Soric, Y. R. Padooru, H. M. Bernety, A. B. Yakovlev, and A. Alù, "Nanostructured graphene metasurface for tunable terahertz cloaking," New J. Phys. **15**, 123029 (2013).
[26] S. Adachi, "Scattering pattern of a plane wave from a magneto-plasma cylinder," IRE Trans. Antennas Propag. **10**, 352 (1962).
[27] J. Palais, "Scattering from a gyrotropic cylinder," IEEE Trans. Antennas Propag. **11**, 505–506 (1963).
[28] V. A. Es' kin, A. V. Ivoninsky, and A. V. Kudrin, "Scattering of an obliquely incident plane electromagnetic wave by a magnetized plasma column: Energy flow patterns at plasmon resonances," Prog. Electromagn. Res. B **63**, 173–186 (2015).
[29] D. R. Biggs, "A study of the dynamic response of plasma filled microwave cavity resonators," Ph. D. dissertation (Stanford University, 2018).
[30] B. Wang, "A theoretical and experimental investigation of plasma photonic crystals and devices," Ph.D. dissertation (Stanford University, 2022).
[31] L. S. Houriez, H. Mehrpour Bernety, J. A. Rodríguez, B. Wang, and M. A. Cappelli, "Experimental study of electromagnetic wave scattering from a gyrotropic gaseous plasma column," Appl. Phys. Lett. **120**, 223101 (2022).
[32] B. Wang and M. A. Cappelli, "A tunable microwave plasma photonic crystal filter," Appl. Phys. Lett. **107**, 171107 (2015).
[33] G. J. M. Hagelaar and L. C. Pitchford, "Solving the Boltzmann equation to obtain electron transport coefficients and rate coefficients for fluid models," Plasma Sources Sci. Technol. **14**, 722–733 (2005).
[34] C. A. Balanis, *Advanced Engineering Electromagnetics* (John Wiley & Sons, 2012).
[35] R. O. Dendy, *Plasma Dynamics* (Oxford University Press, 1990).
[36] See computer simulation technology, microwave studio for www.cst.com.
[37] D. E. Barrick, T. Ruck, W. Stuart, and C. Krichbaum, "Cylinders," in *Radar Cross Section Handbook* (Plenum, New York, 1970), Chap. 4, Vol. 1, pp. 205–339.
[38] B. Wang, R. Sud, M. Leung, M. Yang, J. A. Rodriguez, R. Lee, and M. Cappelli, "OpenEM—electromagnetic field mapping robot for microwave and RF measurements," Hardware X **5**, E00062 (2019).
[39] B. Wang, J. A. Rodríguez, and M. A. Cappelli, "3d woodpile structure tunable plasma photonic crystal," Plasma Sources Sci. Technol. **28**, 02LT01 (2019).